Magnetic Resonance Imaging 56 (2019) 70–76

Contents lists available at ScienceDirect

Magnetic Resonance Imaging

journal homepage: www.elsevier.com/locate/mri

Original contribution

Fast spatially-resolved T_2 measurements with constant-gradient CPMG

Stefan A. Hertel[a,*], Daan W. de Kort[b], Isabelle Bush[b], Andrew J. Sederman[b], Lynn F. Gladden[b], Benjamin Anger[a], Hilko de Jong[a], Matthias Appel[a]

[a] Shell Exploration and Production Inc., Shell Technology Center Houston, 3333 Highway 6 S, 77082 Houston, TX, USA
[b] Magnetic Resonance Research Centre, Department of Chemical Engineering and Biotechnology, University of Cambridge, Philippa Fawcett Drive, Cambridge CB3 0AS, UK

ARTICLE INFO

Keywords:
Core analysis
Porous rocks
Relaxation
CPMG
Fluid typing
Enhanced oil recovery

ABSTRACT

Speed of acquisition is paramount for the application of magnetic resonance to flow experiments through porous rocks. One popular method for imaging core floods is the spatially resolved T_2 experiment which can separate fluids either by their viscosity contrast or by doping one fluid with a relaxation agent. Existing techniques for spatial-T_2 may suffer from long acquisition times and eddy currents due to the pulsing of magnetic field gradients. Here, we propose a constant gradient method for 1d spatially-resolved T_2 which embraces the speed of frequency encoding techniques and avoids eddy currents by the absence of any gradient ramps during the radio frequency (r.f.) pulse train. We provide the operating envelope for this kind of experiment, which is restricted due to the slice selectivity of the r.f. pulses in the presence of the magnetic field gradient. Additionally, we show that the effects of self-diffusion and the mixing of T_1 and T_2 contributions are manageable. As an illustration, we have applied this technique to an enhanced oil recovery experiment. The two fluid phases were tracked without any doping and with a time resolution of 40 s. In this case, the increased time resolution allowed us to observe dynamic flow phenomena such as fluid fingering and the calculation of the velocity of the fluid displacement fronts.

1. Introduction

Magnetic resonance is commonly used in the hydrocarbon industry as a non-invasive tool for measuring fluid distributions in porous rocks and in catalyst supports [1–3]. Among the applications are enhanced oil recovery (EOR) experiments, where one is interested in the displacement efficiency of hydrocarbons by EOR agents as a function of time and location inside reservoir rock [4]. In such studies, the transverse relaxation time (T_2) distribution of the pore fluids provides quantitative fluid typing based on the dependence of T_2 on fluid viscosity or the degree of doping with paramagnetic relaxation agents [3]. Furthermore, it is important to resolve the T_2 spectra spatially, since many interesting phenomena are localized. For example, capillary end effects will cause a spatially varying saturation of the wetting fluid depending on the local pressure drop and truncation effects of the sample [5]. As an illustration of the principle of spatial-T_2, consider Fig. 1, which shows schematically a rock core plug as is commonly used in laboratory core floods. These core plugs measure 2.5 cm in diameter and are up to 5 cm long. The goal of our proposed method is to obtain several T_2 spectra along the axis of the core plug in a time that is short compared to the progression of the front of fluid displacement.

Several techniques exist for the acquisition of spatially resolved T_2 that combine the Carr-Purcell-Meiboom-Gill (CPMG) pulse sequence [6,7] with pulsed magnetic field gradients for spatial encoding [8]. However, for dynamic EOR applications, the temporal and spatial requirements on the pulse sequence are high and include a short total acquisition time, short spin-echo times and millimeter-scale resolution [9]. Typical pulse sequences based on phase encoding gradients increase the total acquisition time with increasing resolution beyond several minutes [8]. This may not always be a problem since most core floods take several days to complete [10]. However, the initial fluid displacement front may progress much faster and long acquisition times may average out interesting saturation effects. Additionally, faster acquisitions allow for more flexibility in synchronizing the execution of the NMR pulse sequence with the fluid injection steps.

Frequency encoding is an alternative approach that reduces acquisition times by encoding all the points simultaneously during one CPMG spin-echo train [11,12]. However, our attempt at implementing the pulse sequence on a permanent magnet system showed that the method suffers from the ramping of the magnetic field gradients, which requires time-consuming balancing and compensation of the induced eddy currents and ultimately increases the minimal spin-echo time. These

---

[*] Corresponding author.
E-mail address: Stefan.hertel@shell.com (S.A. Hertel).

https://doi.org/10.1016/j.mri.2018.09.003
Received 1 September 2018; Accepted 6 September 2018

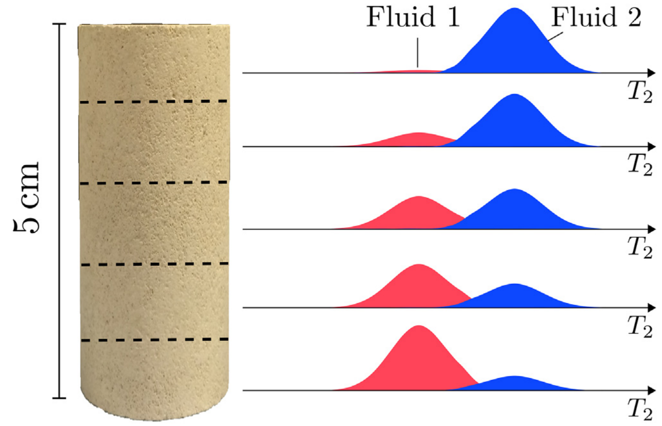

Fig. 1. Principle of spatial-T_2 on the example of a core plug. Horizontal dashed lines separate the subsections along the cylinder axis of the core plug. A T_2 spectrum is obtained for each of these subsections.

obstacles can be overcome by using CPMG in the presence of a constant magnetic field gradient. In this work, we explore the limits of this approach which are imposed by the interaction of the rf-pulses with the magnetic field gradient. We will show that commercial low-field NMR spectrometers which are optimized for short rf-pulse lengths fall within the small window of opportunity where the constant gradient method is viable, and, as an illustration, we will present experiments of a polymer flood of an oil-saturated sandstone.

2. Frequency encoded 1d spatially-resolved T_2: experimental implementation

In spatial-T_2 techniques based on frequency encoding, the NMR signal is acquired in the presence of a pulsed magnetic field gradient G [13,14]. Generally, the gradient is a three-dimensional vector, but in this work, we will exclusively deal with one-dimensional imaging where the gradient is applied along the length of the sample. Hence, all quantities will be expressed as scalars. The pulse sequence used in this work is based on the Carr-Purcell-Meiboom-Gill (CPMG) experiment as shown in Fig. 2 (top). The magnetization is excited by a leading 90° rf-pulse and it is refocused by a train of 180° rf-pulses separated by an inter-echo time of $t_E = 2\tau$.

Fig. 2 (middle) shows the constant gradient as applied in the laboratory reference frame, while Fig. 2 (bottom) shows the effective gradient G^* as experienced by the spin system which is alternating in polarity and continuously refocuses the spin echoes. After the time τ between the leading 90° rf-pulse and the first 180° rf-pulse, the effective gradient has dephased the magnetization and has imposed a wave vector on the magnetization of $k_0 = -(2\pi)^{-1}\gamma G\tau$, where γ is the gyromagnetic ratio. Recording of the first spin echo starts just after the first 180° rf-pulse. Since each spin echo is recorded in its own acquisition window, we assume that the time t is zero at the start of the acquisition and increases to 2τ. Thereafter, the time is reset to zero for the start of the next spin echo. In the presence of the constant magnetic field gradient G, one may express the signal as a function of the wave vector $k = (2\pi)^{-1}\gamma Gt$ instead of just t, which allows us to apply k-space formalism going forward. In this formalism, the signal is given by

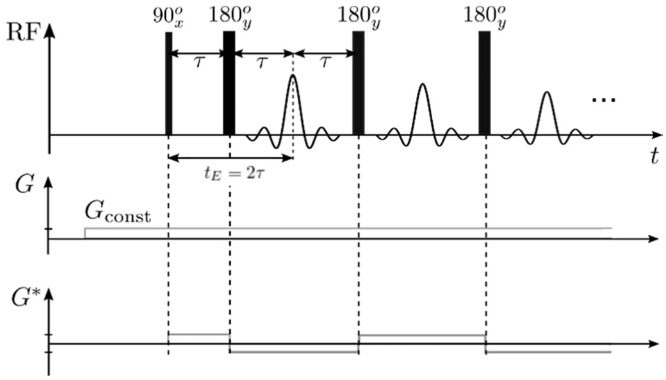

Fig. 2. Pulse sequence of the spatial-T_2 method with a constant gradient. The radio-frequency pulse sequence is based on the CPMG design (top). Pulsed magnetic field gradient as applied in the laboratory reference frame (middle). The effective gradient G^* as experienced by the spin system is alternating in polarity (bottom).

$$S(k) = \int \rho(z)\exp[\mathrm{i}2\pi(k - k_0)]\mathrm{d}z \tag{1}$$

Here, $\rho(z)$ is the one-dimensional profile of the sample, which is equivalent to the hydrogen density as a function of the coordinate z along the length of the sample. Note that the wave vectors $k - k_0$ cancel after a time τ in the middle between the 180° rf-pulses and the maximum signal of the spin-echo is reached. After that the magnetization is again dephased and the process begins anew with the next spin-echo. The profile can be recovered by the inverse Fourier transform, i.e.

$$\rho(z) = \int S(k)\exp[-\mathrm{i}2\pi(k - k_0)]\mathrm{d}k \tag{2}$$

The signal $S(k)$ will be attenuated by T_1 and T_2 relaxation since the excitation with the 90° rf-pulse. For the moment, let us assume that there is only a single T_2 component present in the sample and that this value for T_2 is much larger than the spin echo time $T_2 \gg t_E$. In this case, the magnetization profile will decay as we progress through the CPMG spin echo train according to

$$\rho(z, nt_E) = \rho_0(z)\exp\left(-\frac{nt_E}{T_2(z)}\right) \tag{3}$$

Hence, one may obtain the relaxation time by performing a Fourier transform of each spin-echo followed by fitting the decay of each point of the profile with a single exponential function.

In practice, the signal $S(k)$ is acquired in equidistant time steps and the inverse Fourier transform in Eq. (2) has to be replaced by its discrete version the Discrete Fourier Transform (DFT), which can be solved with the Fast Fourier Transform (FFT) algorithm. Subsequently, the position z will represent one point on the FFT profile and we can analyze the decay of this point as a function of time since excitation. Since we can analyze each point on the profile separately, we can drop the variable z from Eq. (3) going forward.

In rock core systems there is a smooth distribution of relaxation times due to the distribution of pore sizes and thus a single exponential decay as in Eq. (3) is no longer suitable. The decay for one specific point along the sample needs to be replaced by a continuous function such as

$$\rho(nt_E) = \int p(T_2)\exp\left(-\frac{nt_E}{T_2}\right)\mathrm{d}T_2 \tag{4}$$

where $p(T_2)$ is called the T_2 distribution, i.e. the fraction of the magnetization that is decaying with a specific value of T_2. To obtain $p(T_2)$ from the measured decay $\rho(nt_E)$, one needs to perform the inverse of Eq. (4), which is a well-known ill-posed problem. In this work, we employed Tikhonov regularization with the ℓ_2-norm and solved the system of equations with non-linear least squares fitting [15].

To calculate quantitative saturations from $p(T_2)$ one may define a T_2 cut-off which separates the fluids in the T_2 domain. By integrating the NMR signal intensity below the T_2 cut-off one may obtain the volumetric quantity of one of the imbibed fluids

$$V_1 = \int_{T_{2,min}}^{T_{2,cut}} p(T_2)\mathrm{d}T_2 \tag{5}$$

The integral of the NMR signal above the T_2 cut-off will provide the second fluid component, i.e. $V_2 = \int_{T_{2,\ cut}}^{T_{2,\ max}} p(T_2)\mathrm{d}T_2$. Note that the NMR signal has to be calibrated against a known standard before the core flood experiment. Also, the use of a T_2 cut-off is only justified if there is sufficient separation of the peaks in the T_2 spectra between the two fluids. In cases of significant overlaps, one may use multi-Gaussian fits to separate the contribution of each fluid to the overall T_2 spectra.

3. Limitations of the constant gradient approach

3.1. Slice selectivity

With constant gradient CPMG, there is a trade-off between the desire to achieve high resolutions by increasing the magnetic field gradient amplitude and the increasing slice selectivity of the rf-pulses. In case the rf-pulses are slice selective, one may observe a rounding effect on the spatial profile of the sample as well as unrealistically fast relaxation rates at the edges of the sample profile. To minimize this effect, the spectral width of the rf-pulses $\Delta\nu_{\mathrm{rf}}$ must be bigger than the spectral width of the sample

$$\Delta\nu_{\mathrm{rf}} \geq \Delta\nu_{\mathrm{sample}} \tag{6}$$

This relation places an upper bound on the gradient strength, which will be limited by the duration of the rf-pulses t_{p180} and the length of the sample L under study. The two spectral widths are given by $\Delta\nu_{\mathrm{rf}} = 1/t_{p180}$ and $\Delta\nu_{sample} = \gamma GL/2\pi$, respectively. Inserting these two expressions into Eq. (6) and re-arranging yields

$$G \leq \frac{2\pi}{\gamma t_{p180} L} \tag{7}$$

As an example, consider the case of $t_{p180} = 10\ \mu\mathrm{s}$ and a sample length of $L = 5$ cm – then the maximum gradient strength would be $G_{max} = 0.047\ \mathrm{T\ m}^{-1}$. In practice, the rounding effect will be apparent at even lower values, since the spectrum of the rectangular rf-pulse is a sinc function and some degree of rounding is unavoidable. However, experience has shown that lower gradient amplitudes by a factor of two yield satisfactory results.

Eq. (7) shows that NMR spectrometers with very short rf-pulse lengths are at an advantage for constant gradient CPMG. Fortunately, short rf-pulses are a design feature of commercial NMR systems for rock core analysis, since some applications require ultra-short spin-echo times where the length of the rf-pulses becomes a limiting factor.

3.2. Coherence pathways

Conversion of magnetization into coherence pathways (CPs) is intimately linked to the slice selectivity of the rf-pulses [16]. Some portion of the off-resonance magnetization will undergo imperfect rotations, even if the magnetization profile is not noticeably rounded due to slice selectivity. This leads to some magnetization components that are stored along the polarizing magnetic field B_0 for some time intervals. Along B_0, the magnetization is subject to longitudinal T_1 relaxation instead of transverse T_2 relaxation during these time intervals. Subsequent imperfect rotations may recall this portion of the magnetization into the transverse plane where it contributes to the measured signal. This might not be a problem for samples where $T_1 = T_2$, but it could be significant for very viscous fluids or bound fluids in very small pores with $T_1 > T_2$. Additionally, the self-diffusion attenuation is significantly enhanced for parts of the signal that experience long time intervals of storage long B_0 [17]. A detailed analysis of the dominating contributions revealed that 95% of signal is the direct pathway and stimulated echo pathways with one z-storage in between direct echo segments. Hence, most of the signal is decaying with a relaxation time constant close to T_2. In addition to simulations, one may measure the CP spectrum with Phase Incremented Echo Train Acquisition (PIETA) [18], but the analysis of such results may become complex and will be communicated elsewhere. Important for this work is the insight by Song et al. [17] that there is a relaxation rate increase due to self-diffusion which can be as high as 32% over that of the Hahn formula for the specific parameters discussed in the study. Here, the increase may be of the same order of magnitude, but the deviation to bulk measurements does not influence the fluid quantification, if it does not lead to excessive overlap of the T_2 spectra of the two imbibed fluids.

3.3. Diffusion attenuation

Transverse relaxation rates may be enhanced by diffusion of the spin bearing molecules in a magnetic field gradient. In the case of fast exchange, the effective relaxation rate is given by

$$\frac{1}{T_{2,eff}} = \frac{1}{T_2} + \frac{1}{12} D(\gamma G t_E)^2 \tag{8}$$

where $1/T_2$ is the relaxation rate of the fluid imbibed in the pores, which includes the effects of viscosity and surface relaxation in one term. Typical values of $1/T_2$ range between $10^4\ \mathrm{s}^{-1}$ and $10^{-1}\ \mathrm{s}^{-1}$ for rock core systems. The second term in Eq. (8) is the additional apparent relaxation rate caused by the dephasing of the nuclear spins with self-diffusion constant D in the gradient G. As an approximation of the order of magnitude of this term we consider the self-diffusion of water at room temperature of $D = 2 \times 10^{-9}\ \mathrm{m^2 s^{-1}}$ [19]. Furthermore, the longer the spin echo time, the higher is the influence of self-diffusion according to Eq. (8). Here, we may assume an upper limit of $t_E \leq 1$ ms which is large for studying rock cores and a constant gradient of $G = 0.05\ \mathrm{Tm}^{-1}$ close the limit found in the previous subsection. Given these assumptions, the relaxation rate due to diffusion as given by the second term in Eq. (8) will be $R_D = 7.4\ 10^{-4}\ \mathrm{s}^{-1}$. This value is three orders of magnitude lower than the lowest relaxation rates usually found in rock core systems. Therefore, self-diffusion is not a limiting factor for the applications studied in this contribution. There is even some room for cases, where the values of D are much higher e.g. if the experiments are performed at high temperatures or with oils that contain a large amount of dissolved gas.

4. Experimental

4.1. Core flooding system

Core flooding systems are carefully engineered to ensure that the fluid dynamics in the rock core resemble the dynamics in the oil field. For example, they are optimized for very small volumetric flow rates and they generally allow to apply an external confining pressure to the sample to simulate the reservoir stresses. In this work, we combined a home built fluid injection system with a commercially available pressure cell with an integrated r.f. coil. Fig. 3 shows schematically the NMR spectrometer with the pressure vessel and fluid injection tubing. The pressure vessel was an Oxford Instruments Inc. overburden cell. The core plug was held in place by PEEK end caps, which were placed on both sides of the core plug and were fixed in place by Teflon shrink wrap. The assembly was centered in the middle of the inbuilt rf-coil by monitoring the one-dimensional profile with the NMR spectrometer. The overburden cell allowed for a maximum confining pressure of 5000 psi, which will be important for future applications which mimic reservoir conditions. In this work, we opted for a confining pressure of 1000 psi to seal the sample within the Teflon shrink wrap.

Core flooding was performed by injecting fluids from the top and collecting the effluent in a beaker at the bottom of the pressure vessel. Two separate core flooding experiments were performed. The first was a so-called drainage experiment where the core plug is initially fully saturated with the wetting fluid, which is gradually displaced by the non-wetting fluid until a stable saturation is established. This procedure is often applied to prepare the core plugs to a state that mimics the fluid distributions in the field. The second core flood was designed to mimic an enhanced oil recovery process.

During the drainage experiment, a porous plate is inserted on the

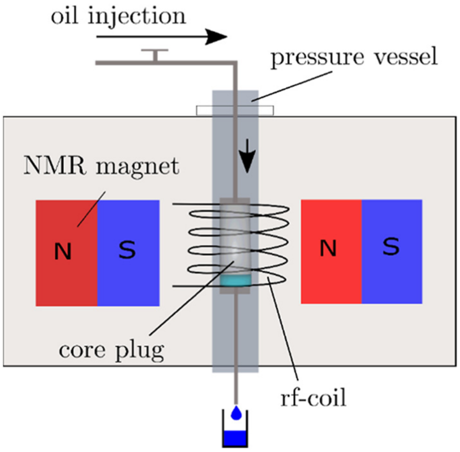

Fig. 3. Sketch of the core flooding setup. The pressure vessel was integrated into the NMR spectrometer and viscous paraffin oil was injected from the top, while the effluent brine was collected in a beaker.

effluent side of the setup. The porous plate is made of a microporous ceramic which is impermeable to the non-wetting fluid (in this case oil or paraffin) up to a certain injection pressure [20]. This pressure equals the entry pressure of the porous plate and corresponds to the oil-brine capillary pressure in the rock [20]. In this work, we desaturated at a capillary pressure corresponding to the maximum entry pressure of the porous plate of 15 bar. The displacement of brine by paraffin was observed until a homogeneous saturation was established along the length of the core plug. The paraffin oil was injected at a volumetric flow rate of $\dot{V} = 0.03\ \mathrm{mL/min}$. The entire flood lasted 4 h and a spatial T_2 map was acquired every 40 s.

The second set of experiments was designed to study the displacement efficiency of a polymer EOR agent over the recovery by just flooding the plug with low salinity brine. Hence, the first step was to flood the oil saturated core plug with brine until there was no further oil production. The production was monitored both by measuring the effluent and by observing the spatial-T_2 spectra as a function of time. Once completed, a polymer solution was injected, followed by a second period of brine injection until no further production was observed. The initial brine flow rate for imbibition (injection of the wetting fluid) was $\dot{V} = 0.03\ \mathrm{mL/min}$. Flow was imposed for 17.5 h and a spatial T_2 map was recorded every 160 s. It was followed by polymer injection at 0.03 mL/min for 2.5 h. The polymer injection was followed up by a second brine flood, which was supposed to push the polymer fluid front through the porous rock. The secondary brine flood was carried out for 15.6 h at a flow rate of 0.03 mL/min.

It is interesting to note that the evaluation of the data for the entire EOR core flood involved the inversion of a total of 765 spatial T_2 maps with 46 points each. Hence, we performed roughly 35,000 inversions, which was only possible with an automated data shaping and interpretation program. We chose to write the data handling, Fourier transform, our in-house inversion, and the plotting of the final figures in the programming language Python.

4.2. NMR implementation

The NMR experiments were carried out on an Oxford Instruments spectrometer with a ^{1}H Larmor frequency of $\nu_0 = 2.3$ MHz. The 90° and 180° rf pulse lengths were 6 µs and 12 µs, respectively. The applied constant gradient was $G_{\mathrm{const}} = 0.018$ T/m. This gradient amplitude is at the upper limit where the slice selectivity of the rf-pulses was within the limit set by Eq. (7) less a factor of two. The dwell time was set to $dw = 10\ \mu s$. This resulted in a field of view of $FOV = 12.83$ cm. A total number of points of $SI = 46$ was acquired for every spin-echo which yielded a resolution of $res = 2.79$ mm. The spin-echo-time was $t_E = 0.6$ ms and the number of echoes was $N_{ech} = 3{,}500$. The recycle delay of $RD = 5$ s allowed for a shortest total acquisition time of 40 s when the number of scans was set to $NS = 8$.

In our implementation of the pulse sequence, the applied constant gradient G_{const} is switched on a time t_{settle} before the excitation rf-pulse. This settling time is needed for the eddy currents, which can be induced due to the initial ramp up of the magnetic field gradient, to decay. This time is specific for each NMR spectrometer. For our system based on a permanent magnet design, we found that $t_{\mathrm{settle}} = 10$ ms is sufficient. This value was established by observing the Fourier transform spectra of the first ten spin echoes and adjusting t_{settle} until no phase distortion between the spin echoes was observable and by ensuring that the first spin echo maximum was occurring exactly halfway between the first two 180° rf-pulses. It is worth noting that the pulse sequence was also optimized to ensure that all the following spin-echo maxima were occurring at the same time up to a tolerance of one dwell time dw in the acquisition window. Failure to adjust the pulse sequence timing to such a high accuracy resulted in distorted Fourier transform profiles and higher apparent relaxation rates.

The minimum spin-echo time $t_{E,\ min}$ was limited by the number of sampling points acquired SI and the dwell time dw between each sampling point. The total time needed for acquisition is given by

$$t_{E,min} = t_{filter} + SI\ dw + t_{180} + 0.5\ dw \tag{9}$$

where t_{filter} is the dead time of the digital filter which was 35 μs for our system. With the parameters given above the minimum spin echo time was $t_{E,\ min} = 0.512$ ms. Note that the main limitation of the echo time is the number of points recorded N_s and the dwell time dw. We found that there is some room for adjustment if smaller values for t_E are required. For example, some r.f. coils have shorter r.f. pulse lengths, which allows for an increase of the constant gradient G_{const}. Thus, one may obtain the same resolution with either less points, or a decrease in the dwell time. For a system with $t_{180} = 10$ µs instead of $t_{180} = 12$ µs this may allow for $t_{E,\ min} = 0.4$ ms.

4.3. Materials

Two rock core plugs were used for the two separate experiments. Both plugs B1 and B2 were Bentheimer sandstone purchased from Kocurek Industries Inc. They were drilled from a solid block with a cylindrical drill of 1 in. ($d = 2.54$ cm) diameter and subsequently cut to a length of $L_1 = 4.44$ cm and $L_2 = 4.46$ cm, respectively. The porosities were $\Phi_1 = 22\%$ and $\Phi_2 = 21\%$. The dry core plugs were vacuum saturated with 30 kppm NaCl brine. The model oil was the paraffin N100 which is manufactured by Cannon Instrument company and is commonly used as a viscosity reference standard. The paraffin had a viscosity of 200.2 cP at $T = 25$°C. The polymer solution for the enhanced oil recovery part of the experiments was FLOPAAM™ 3230 s manufactured by SNF Inc. The dry polymer powder was mixed by weight with brine to a target viscosity of 28 cP at 25°C at a shear rate of 10 s^{-1}. The final concentration of polymer was 1.5 g of dry FLOPAAM™ 3230 s + 1 g NaCl in 1 L of deionized water.

5. Results and discussion

5.1. Drainage core flood

Fig. 4 shows spatial-T_2 images at three time points after starting the injection of oil into the brine-saturated Bentheimer sandstone B1. The sketch to the left shows schematically the core plug with the porous plate and the direction of flow. In all three subfigures the white dashed line indicates the separation of the oil and brine by the T_2 cut-off at $T_{2,\ cut} = 200$ ms. Fig. 4 a) was acquired at the beginning of the oil injection. Fig. 4 b) shows the progression of the fluid front where the brine in the top half of the core plug has already been displaced by oil. Fig. 4 c) shows the core plug at the end of the desaturation experiment. One

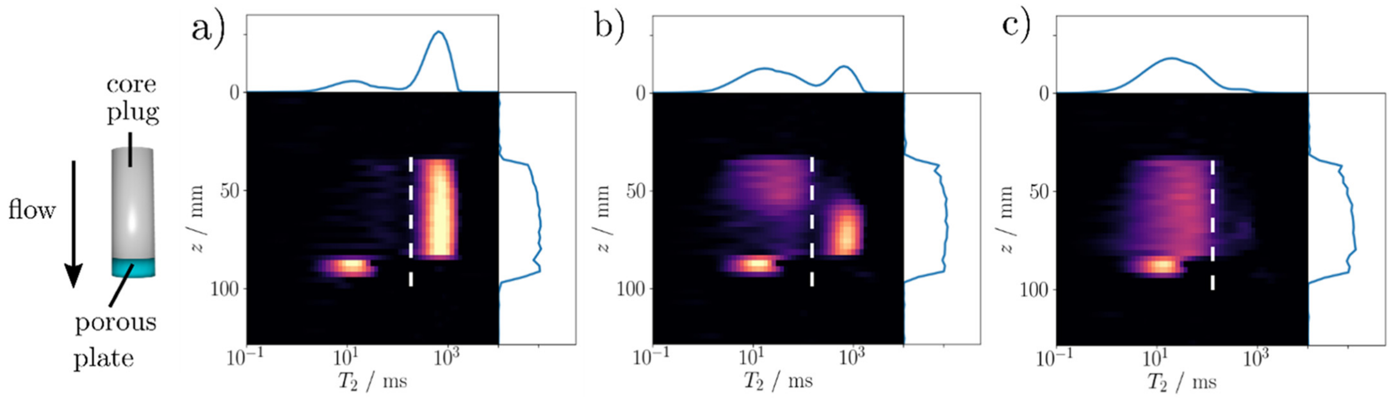

Fig. 4. Spatial-T_2 images showing the displacement of brine (T_2 = 200 ms–1 s) by paraffin (T_2 = 1 ms–200 ms). The sketch on the left is showing the flow direction of paraffin and the location of the porous plate. a) Fully brine-saturated core plug, b) Shortly after the start of paraffin injection (flow from top to bottom). Paraffin front moving downwards displacing the brine. c) Residual water saturation and nearly homogeneous oil saturation after core flood completed. In all three spatial-T_2 images the white dotted line indicates the location of the T_2 cut-off at 200 ms.

constant feature of all three T_2 maps is the signature of the porous plate. The brine inside the porous plate is confined by micropores and therefore the relaxation time is short ($T_2 \approx 10$ ms) compared to the brine inside the Bentheimer sandstone. Since the paraffin cannot enter the porous plate, it does not change its T_2 relaxation time throughout the drainage experiment.

At each time step during the core flood, we extracted quantitative information about the local saturation by integrating the intensity in the spatial-T_2 spectra for each pixel along the sample axis according to Eq. (5). Fig. 5 (top) shows the saturation of the two fluids at the time t = 0.2 h after the start of the drainage experiment corresponding to the spatial-T_2 map shown in Fig. 4 a). The location of the porous plate is indicated by the grey shaded area. One may observe the onset of displacement of brine (blue, dashed) by oil (red, dash dotted) at the entry of the sample. The sum of both fluids (black, solid) reveals some residual rounding due to the slice selectivity of the r.f. pulses.

Due to the high time resolution of Δt = 48 s (8 s were used by our system to save the data) one may calculate a time derivative of the saturation profile. This numerical time derivative can be obtained by subtracting two saturation profiles at different instances in time according to

$$\dot{V}(z) = \frac{\Delta V(z)}{\Delta t} = \frac{V(z, t_2) - V(z, t_1)}{t_2 - t_1}, \; t_2 > t_1 \tag{10}$$

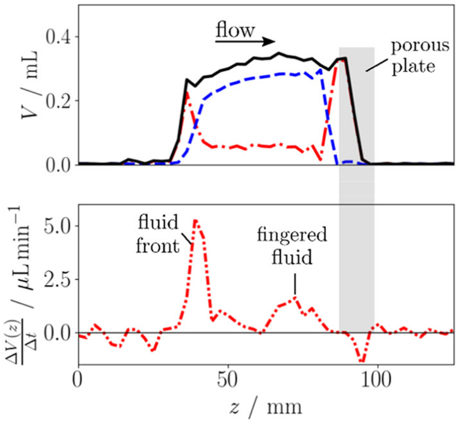

Fig. 5. (top) Snapshot of the spatially resolved saturation of oil (red - · -), brine (blue - - -) and the sum of both fluids (black —). This saturation profile was derived from the spatial-T_2 map at time t = 0.2 h after the start of the drainage experiment corresponding to the spatial-T_2 map shown in Fig. 4 a). (bottom) Numerical time derivative showing the local volume change per unit of time of the oil phase (red - · · -). Note the curve does not show the local flow rate of oil, but rather the change in local oil saturation due to build-up of oil locally and the displacement of an equivalent amount of brine.

Due to noise on the saturation profiles, one may have to apply an averaging step before Eq. (10) can be applied. Here, we chose to apply a moving average of seven saturation profiles and to subtract two profiles separated by seven snapshot acquisitions. Hence, the time difference between these two snapshots was $t_2 - t_1$ = 5.6 min. Fig. 5 (bottom) shows the result of this analysis for the profile shown in Fig. 5 (top). One may observe that the largest change of oil saturation (red, dash dotted) is occurring just in front of the oil fluid front. Interestingly, there is a second peak just in front of the porous plate. This peak is showing that the oil saturation is increasing locally, while the center of the sample is seeing little change. One explanation for this behavior is that the paraffin oil is channeling through the largest pore throats. Once the channeling oil is arriving at the location of the porous plate it is not progressing, since the porous plate is impermeable for the paraffin. Therefore, the oil is staying in the sample and building up locally just in front of the porous plate. Note that this process is different from the effect of viscous fingering, where a fluid with lower viscosity is channeling through a fluid with higher viscosity. Here, the viscosity relationship is the reverse, and the effect may be occurring due to the presence of a large difference in pore sizes between the largest and smallest pores in the sample.

As another example, the profile in Fig. 6 (top) is calculated from the spatial-T_2 map acquired later in the core flood at time t = 3 h and which was previously shown in Fig. 4 b). The arrow indicates the direction of flow of the oil injection and the local volume of oil is shown with the red, dash dotted line. As the brine (blue, dashed) is expelled from the core plug the saturation changes and there is an inhomogeneous distribution of brine along the length of the sample at that particular point in time. While the entry side of the sample is already fully oil saturated, the other half of the sample is still experiencing the displacement process. It is interesting to see that the displacement front is a smooth distribution at this stage in the core flood, and that there is some oil present up to the outlet of the sample. This may be a consequence of oil displacing the brine first inside the largest pores with the largest connected pore throats due to the process shown in Fig. 5. This displacement is then followed by the displacement front inside the smaller pore network as the local pressure increases.

Fig. 6 (bottom) shows the time derivative of the oil saturation at time t = 3 h. The hold-up of the oil in front of the porous plate causes the saturation to change both in front of the plate and over a broad region over half the length of the sample. It appears that the fluid displacement front is much broader than the front in Fig. 5 (top). This feature of a more diffuse oil front can also be seen in the saturation

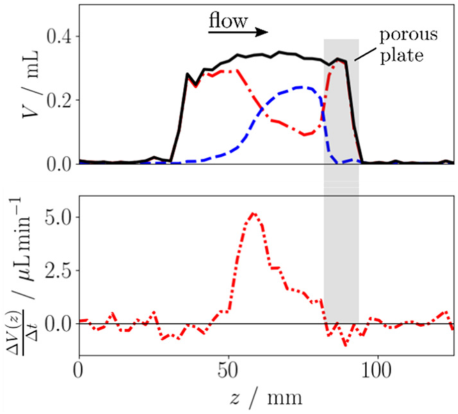

Fig. 6. (top) Snapshot of the spatially resolved saturation of oil (red - · -), brine (blue - - -) and the sum of both fluids (black —). This saturation profile was derived from the spatial-T_2 map at time $t = 3$ h. The arrow indicates the direction of flow of the oil injection. The shaded grey region indicates the location of the porous disc. The saturation profile was calculated from the spatial-T_2 profile shown in Fig. 4 b). (bottom) Time derivative showing the local volume change per unit of time of the oil phase (red - · · · -).

profile shown in Fig. 6 (top). Additionally, the broadening effect due to the moving average of seven profiles should be present in both figures. Thus, one is observing true fluid dynamics effects which may be used in the future for a more complex analysis of the efficiency of displacement processes and comparisons to fluid dynamics simulations.

5.2. Enhanced oil recovery core flood

A fully oil saturated core plug was used for the EOR experiment as opposed to a fully brine saturated core plug for the experiment discussed in the previous section. An initial spatial-T_2 map showed that the residual brine saturation was homogeneous along the length of the sample. Fig. 6 shows the total amount of fluid present in the core plug at each time point. Only every tenth point is shown in the plot and the time resolution was $\Delta t = 2.8$ min. The three stages of the core flood are separated by the vertical dashed lines. The primary waterflood at the time interval $t = 0 - 17.7$ h was followed by the polymer injection which was started at $t = 17.5$ h and lasted for ca. 2.5 h. The polymer injection was followed by a secondary waterflood which was sustained until no change in saturation was observed from $t = 20 - 35.6$ h.

During the initial stages of the primary waterflood, the oil saturation decreases rapidly from ca. 4 mL to 2.7 mL (red, dots). It is followed by a more gradual oil production until an equilibrium oil saturation of 2.5 mL. The vertical dashed line indicates the start of the polymer injection, which caused another drop in oil saturation followed by a gradual decline to ca. 2.3 mL at the end of the core flood. Fig. 8 shows the saturation profile at time $t = 18.7$ h which is highlighted in Fig. 7 with the large dot and the large triangle. The oil profile shows a local maximum, which is moving through the core plug. The direction of the movement of the oil bank is indicated by the arrow. The oil saturation in front of the oil bank is higher than at the inlet of the sample.

By analyzing several consecutive saturation profiles, one may extract the approximate position of the oil bank $z_{oil,\ max}(t)$ by picking the point of maximum oil saturation at each instant in time during the polymer flood. This analysis allows for the approximation of the velocity with which the oil bank is moving through the core plug. The resulting apparent velocity of the oil bank is $v_{oil} = \frac{\Delta z_{oil,max}}{\Delta t} = 0.4 \pm 0.05$ mm min^{-1}. Here, the uncertainty of approximately 12.5% was estimated by analyzing several different saturion profiles with varying time separations. The resulting variation in velocities was caused mainly by experimental noise on the profiles, which affected the location of the saturation maxima. The volumetric flow rate in our experiments was set to approximate a superficial fluid velocity as found in an oil field of $v_{field} = 1\text{ft day}^{-1} = 0.21$ mm min^{-1}. This superficial fluid velocity should be achieved if the whole cross-section of the core plug were available for flow. However, in the saturation profile shown in Fig. 8, one may observe a high residual brine saturation of approximately $S_w = 50\%$. Hence, only ca. 50% of the pore space is available for the flow of oil through a continuous connected fluid phase, which makes the apparent velocity of the oil bank of twice the superficial flow velocity plausible.

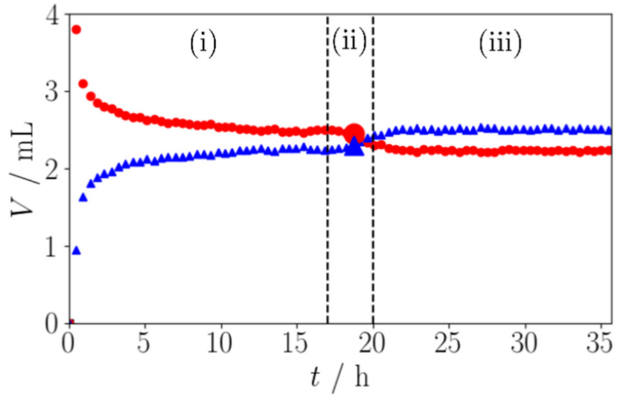

Fig. 7. Saturation of oil (red ●) and brine (blue ▲) integrated over the whole core plug as a function of time. The three stages of the oil recovery process are separated by vertical dashed lines. (i) Primary waterflood, (ii) polymer injection and (iii) secondary waterflood. The highlighted markers indicate the instant of time used for the extraction of a saturation profile shown in the following Fig. 8.

6. Conclusions

The time resolution with the presented approach was on the order of 40 s if 8 scans were averaged and a recycle delay of 5 s was applied. Additionally, the minimal echo spacing can be reduced to $t_E = 0.4$ ms, which is comparable to downhole NMR logging tools and low compared to current spatial-T_2 techniques. In this experiment, the highest resolution without distortion of the 1d-MRI profile was 2.79 mm; less than what could be achieved using phase imaging methods such as SE-SPI, but sufficient to observe end-effects and core plug heterogeneities. The high temporal resolution of $\Delta t = 40$ s extends our ability to investigate the dynamics of saturation changes during core flood experiments. For example, we were able to observe fluid fingering, fluid hold up as well as the movement of an oil bank during the polymer core flood. Additionally, the quantitativeness of low field NMR allows for the calculation of various important parameters such as local saturation changes as a function of time. As an outlook, one may extend the

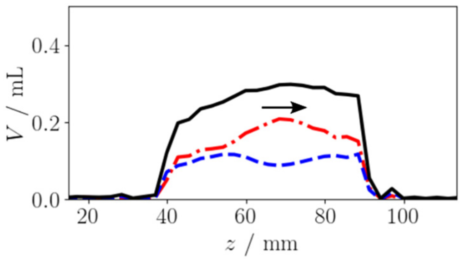

Fig. 8. Saturation profile (black — **solid line**) during the polymer injection stage of the EOR core flood. The arrow shows the direction of flow. The oil saturation (red - · -) shows the location of the oil bank moving through the core plug. The brine saturation (blue - - - **dashed line**) at the location of the oil bank is lower due to the higher local oil saturation. Note that the polymer appears at similar T_2 relaxation rates as the brine and therefore, it is included in the brine saturation after the oil bank has moved through the rock.

constant gradient approach to spatially resolved T_1-T_2 correlation experiments. This extension would allow for the fluid separation for systems where the T_2 contrast is not high enough to separate two fluid phases and doping is not an option due to concerns of the chemical impact of such substances.

Acknowledgments

We would like to thank Ian Nicholson from MRF Innovations Ltd. for help with the pulse sequence design and implementation. Shell International E&P Inc. is thanked for permission to publish the results of this study.

References

[1] Watson AT, Chang CT. Characterizing porous media with NMR methods. Prog NMR Spec 1997;31:343–86. https://doi.org/10.1016/S0079-6565(97)00053-8.

[2] Mitchell J, et al. Magnetic resonance imaging in laboratory petrophysical core analysis. Phys Rep 2013;526:165–225. https://doi.org/10.1016/j.physrep.2013.01.003.

[3] Mitchell J, Fordham E. Nuclear magnetic resonance core analysis at 0.3 T. Rev Sci Instrum 2014;111502:85. https://doi.org/10.1016/j.physrep.2013.01.003.

[4] Green DW, Willhite GP. Enhanced oil recovery. Society of Petroleum Engineers; 1998.

[5] Hadley GF, Handy LL. A theoretical and experimental study of the steady state capillary end effect. Soc Pet Eng 1956. https://doi.org/10.2118/707-G.

[6] Carr HY, Purcell EM. Phys Rev 1954;94:630–8. https://doi.org/10.1103/PhysRev.94.630.

[7] Meiboom S, Gill D. Rev Sci Instr 1958;29:688–91. https://doi.org/10.1063/1.1716296.

[8] Muir C, Balcom BJ. Magn Reson Chem 2013;51:321–7. https://doi.org/10.1002/mrc.3947.

[9] Li M, Romero-Zeron L, Marica F, Balcom BJ. Energy Fuel 2017;31:4904–14. https://doi.org/10.1021/acs.energyfuels.7b00030.

[10] Mitchell J, et al. Real-time oil-saturation monitoring in rock cores with low-field NMR. J Magn Reson 2015;256. https://doi.org/10.1016/j.jmr.2015.04.011.

[11] Mitchell J, et al. Quantitative in situ enhanced oil recovery monitoring using nuclear magnetic resonance. Transp Porous Media 2012;94. https://doi.org/10.1007/s11242-012-0019-8.

[12] Mitchell J, et al. Monitoring chemical EOR processes. Soc Pet Eng 2014;3. https://doi.org/10.2118/169155-MS.

[13] Callaghan PT. Principles of nuclear magnetic resonance microscopy. Oxford, UK: Oxford University Press; 1991.

[14] Majors P, Li P, Peters E. NMR imaging of immiscible displacements in porous media. SPE Form Eval 1997;12:164–9. https://doi.org/10.2118/30557-pa.

[15] Mitchell J, Chandrasekera TC. Understanding generalized inversions of nuclear magnetic resonance transverse relaxation time in porous media. J Chem Phys 2014;141:224201https://doi.org/10.1063/1.4903311.

[16] Hürlimann MD. J Magn Reson 2001;148:367–78. https://doi.org/10.1006/jmre.2000.2263.

[17] Song YQ. Categories of coherence pathways. J Magn Reson 2002;157:82–91. https://doi.org/10.1006/jmre.2002.2577.

[18] Hertel SA, Galvosas P. J Magn Reson 2017;275:90–7. https://doi.org/10.1016/j.jmr.2016.12.006.

[19] Holz M, Heil SR, Sacco A. Temperature dependent self-diffusion coefficients of water and six selected molecular liquids for calibration in accurate ^{1}H NMR PFG-measurements. Phys Chem Chem Phys 2000;2:4740. https://doi.org/10.1039/b005319h.

[20] McPhee C, Reed J, Zubizarreta I. Core analysis a best practice guide. Developments in petroleum science. Vol. 64. Amsterdam, The Netherlands: Elsevier; 2015.